Journal of Materials Research and Technology 35 (2025) 1358–1368

Contents lists available at ScienceDirect

Journal of Materials Research and Technology

journal homepage: www.elsevier.com/locate/jmrt

# Influence of base plate preheating temperature on fatigue strength of AISI 4140 manufactured by laser powder bed fusion

Philipp Schüßler *, Benjamin Dollhofer, Christian Krämer, Lukas Englert, Frauke Hinrichs, Volker Schulze, Stefan Dietrich

*Institute for Applied Materials - Materials Science and Engineering (IAM-WK), Karlsruhe Institute of Technology (KIT), Karlsruhe, 76131, Germany*

ARTICLE INFO

*Keywords:*
Laser powder bed fusion
Additive manufacturing
AISI 4140
42CrMo4
Fatigue
Mechanical properties

ABSTRACT

This study investigates the influence of base plate preheating temperature on the fatigue performance of additively manufactured AISI 4140 steel, manufactured through laser powder bed fusion (PBF-LB). By varying preheating temperatures (150 °C, 300 °C, and 450 °C), distinct microstructures – martensitic, mixed martensitic-bainitic, and fully bainitic – were achieved, each influencing fatigue strength and toughness. The results show that a fully martensitic structure provides superior fatigue resistance, while the mixed microstructure batch displayed reduced toughness and fatigue strength due to tempered martensite embrittlement (TME), which occurred at lower hardness compared to conventionally treated steels. However, the fully bainitic batch exhibited the highest toughness and a fatigue resistance between the two other batches, confirming that bainitic autotempering occurs at elevated temperatures, without evidence of embrittlement. Additionally, inherent porosity in AM samples acted as a stress concentrator, further reducing fatigue performance. This study highlights the importance of optimizing the base plate preheating temperature to control microstructure and porosity for enhanced fatigue performance in additively manufactured AISI 4140 components.

## 1. Introduction

In recent years, laser powder bed fusion (PBF-LB) has emerged as an essential additive manufacturing (AM) process for producing structural and tailored metallic components with high geometric complexity. This capability has fueled the rapid adoption of PBF-LB across various industries. Despite its advantages, process-related residual stresses, high surface roughness and intrinsic porosity can significantly reduce load bearing capacity compared to conventionally cast and shaped materials [1–4]. Furthermore, the microstructure that develops during the process has a decisive influence on fatigue behavior, as is the case for conventionally manufactured components [1,3,5]. In order to advance technology at the same swiftness as before, these correlations must be fully understood.

The development of process-related residual stresses is due to the complex temperature history of AM components. Their formation during the AM process is related to the temperature gradients in the component and melt pool. Therefore, residual stresses are dependent on both the process parameters and the geometry of the components. However, elevated residual tensile stresses have generally been observed close to the surface of the component [4,6]. In addition, defects near the surface, such as pores and rough textures of partially melted powder, have a particularly strong impact on reducing the fatigue strength of AM components [1,2,7,8]. To address these issues, several studies on additive manufacturing (AM) of carbon steels aim to reduce porosity [3,9–12] and cracks [3,11,13], as well as improving static mechanical properties [3,12,14]. As intrinsic porosity is a common weakness in additively manufactured components, mechanical surface treatments and hot isostatic pressing are already used to effectively reduce surface porosity [15,16]. Furthermore, mechanical treatments improve fatigue properties by increasing hardness through grain refinement and enhanced dislocation density, as finer grains contribute to higher yield stress in metals according to the Hall–Petch equation [17]. The microstructure of high-carbon steels, such as AISI 4140, presents unique challenges compared to those of low-carbon steels, mainly due to martensitic transformations during cooling. This transformation induces high localized stresses, increasing the likelihood of cold cracking from volume changes during the phase transition [14,18,19]. Optimizing process parameters such as scan speed, laser power and laser spot size were able to prevent microcracking for AISI 4140, but significantly reduce the usable process window [20]. Preheating the base plate has proven to be an effective approach to reduce crack susceptibility and slightly broaden the process window for high

* Corresponding author.
*E-mail address:* philipp.schuessler@kit.edu (P. Schüßler).

https://doi.org/10.1016/j.jmrt.2025.01.073
Received 13 December 2024; Accepted 9 January 2025
Available online 16 January 2025

carbon steels [21,22]. In addition, the complex thermal history of components during additive manufacturing can significantly alter the resulting microstructure. Varying quenching rates may result in bainitic or martensitic microstructure, depending on the process strategy [23]. Due to the addition of preheating to the base plate, the microstructure undergoes cyclic austempering or autotempering depending on the preheating temperature. Chen et al. [24,25] demonstrated that in AISI 4130, differing bainitic volume fractions within homogeneous mixed microstructure significantly influence the fatigue strength of the components. The bainitic microstructure is also known to be more resistant to temperature with respect to tempering effects than the martensitic microstructure due to its higher formation temperature [26,27]. In contrast, the martensitic microstructure is recognized for experiencing tempered martensite embrittlement (TME) when subjected to tempering within the anticipated temperature range 200 °C to 400 °C [28,29]. In order to be able to precisely determine the influence of the microstructure on the fatigue properties, it is therefore necessary to understand the complex history of its formation due to the AM process.

This publication aims to answer the question of the extent to which variation in base plate temperature affects the fatigue properties of AM components. Further, the influence of porosity and microstructure differences of components manufactured using AM compared to conventionally manufactured components was investigated. To address this inquiry, an investigation was conducted on three distinct groups of AM samples, each subjected to a different base plate temperature. In addition, a control group was included, produced using conventional manufacturing methods. The goal here was to isolate and examine the specific impact of porosity and microstructure on the service life of components in comparison to the AM groups. In order to reduce the influence of surface roughness and improve comparability across the various batches, minimizing geometric variances, all samples were machined. Initially, the sample groups were subjected to a metallographic examination that included density, surface roughness, and hardness measurement. The further characterization of the microstructure was performed using SEM and EBSD imaging. In addition, X-ray diffraction measurements were used to analyze the retained austenite content and residual stresses within the sample. Subsequently, tensile tests were performed to determine their static mechanical properties. The fatigue strength of each sample group was evaluated through moment-controlled rotational bending fatigue tests, generating SN-curves with the corresponding statistical analysis. Finally, the material properties were correlated with observed porosity and microstructure, offering valuable insights into the process-dependent fatigue behavior of additively manufactured components.

## 2. Material and methods

### 2.1. Material

An inert gas atomized pre-alloyed AISI 4140 (german grade 42CrMo4) powder was used to manufacture the specimens through the PBF-LB process. Control specimens were manufactured out of conventionally fabricated AISI 4140 rods. The chemical composition of the powder, the parts manufactured by additive manufacturing and the control specimens are listed in Table 1. The chemical composition was measured with the inductively coupled plasma optical emission spectroscopy (ICP-OES) method for Mn, Cr, Si, Mo, and Fe and an elemental CS-Analyzer for C.

### 2.2. Specimen processing

The specimens for this study were divided into four groups, each representing a distinct processing route. The as-built and machined geometries of the specimens are illustrated in Fig. 1, where (a) visualizes the as-built state after the AM process, and (b) the standardized cylindrical geometry after machining. The machined geometry was consistent across all batches, facilitating a controlled comparison of fatigue properties across the different process routes. The build direction (BD) is marked for the AM specimens, while the conventionally manufactured specimens were machined to identical dimensions.

**Table 1**
Chemical composition of the powder, as-built AM parts and the Control batch in wt.%.

| | C | Mn | Cr | Si | Mo | Fe |
|---|---|---|---|---|---|---|
| Powder | 0.39 | 0.76 | 1.09 | 0.34 | 0.25 | bal. |
| AM | 0.38 | 0.75 | 1.17 | 0.40 | 0.29 | bal. |
| Control | 0.43 | 0.77 | 1.15 | 0.27 | 0.21 | bal. |

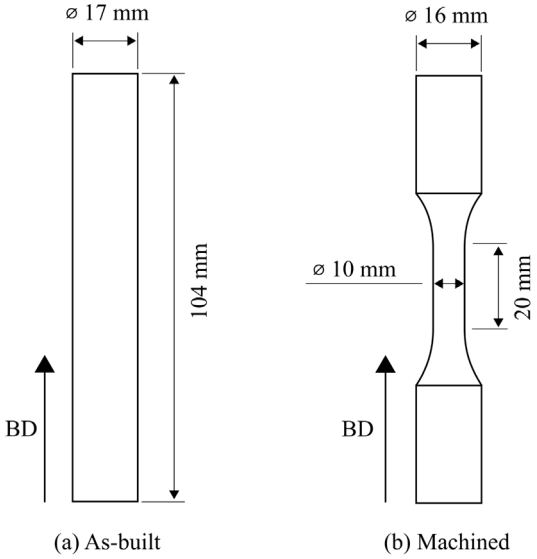


**Fig. 1.** Technical drawing for (a) the as-built specimens after the AM process and (b) the specimens after machining. The build direction is marked for the AM specimens; the conventionally manufactured specimens were machined to the same dimensions.

To analyze the effects of base plate preheating temperature on fatigue performance, three batches of 36 cylindrical rods (diameter 17 mm) were manufactured. All AM batches were manufactured by Jell GmbH & Co. KG (Germany) on a ConceptLaser M2 (GE Additive, USA) PBF-LB machine. Throughout the study, the laser parameters and scanning strategy were kept constant: a laser power of 350 W, spot size 175 µm, scan speed 800 mm s$^{-1}$, hatch distance 110 µm, and layer thickness 50 µm, applying a stripe strategy. The stripe strategy utilized a bidirectional laser scan path with a stripe width of 5 mm, a scan pattern rotation of 72° per layer, and a single perimeter line. This study's unique approach diverges from traditional methods by isolating base plate preheating temperature as the sole variable, maintaining all other processing parameters constant. This enables a focused investigation into the microstructural effects on fatigue performance, a key differentiator from previous studies. The base plate preheating temperatures were set to 150 °C (AM150-M), 300 °C (AM300-M), and 450 °C (AM450-M). After the AM process, the samples were machined to their final shape. To enable direct comparison between the AM150-M batch and conventionally manufactured specimens, a control batch was prepared by machining samples from a rod (Control-QT-M). These samples were heat treated and machined to match the geometry and hardness of the AM specimens. The heat treatment parameters, determined using the Hollomon–Jaffe equation, consisted of austenitization at 850 °C for 30 min in a vacuum oven, quenching in oil, and tempering at 450 °C for 2 h. After the heat treatment, the samples were machined to achieve their final shape.

### 2.3. Experimental methods

#### 2.3.1. Metallographic characterization

The density of each specimen was analyzed according to Archimedes' principle with the precision scale ME503TE (Mettler Toledo,

USA) and water as the medium for the measurements. A dispersive agent was used to reduce the surface tension. All density measurements were conducted after the specimens were machined to their final geometry. To thoroughly examine the pore distribution and structure, one sample underwent micro-tomographic ($\mu$CT) imaging. The $\mu$CT scan was carried out using a YXLON Precision $\mu$CT (YXLON International GmbH, Germany), set at an acceleration voltage of 200 kV and a target current of 0.24 mA. For the image reconstruction, 3000 projections were captured during a full 360° rotation on a Perkin Elmer XRD1620 AN flat panel detector, which had a resolution of 2048 px × 2048 px and a pixel pitch of 0.2 mm. The samples were imaged with a focus object distance (FOD) of 36.25 mm and a focus detector distance (FDD) of 900 mm, achieving a voxel size of 8 µm. To reduce noise in the projection images, a detector integration time of 1 s was used, coupled with the binning of two frames. Image reconstruction was performed using the filtered backprojection (FBP) algorithm within VGStudioMAX 2022.4 (Volume Graphics International GmbH, Germany). Additionally, a median filter was applied for noise suppression. Porosity was analyzed using the VGEasyPore module in VGStudioMAX.

The surface roughness was analyzed by the confocal microscope $\mu$surf (NanoFocus, Germany) after the machining process. The line based analysis was carried out along the axial direction of the samples with a line length of 3.77 mm. In order to characterize the hardness profile and the microstructure of each batch, the specimens were cut in axial direction (XZ plane) as well as normal to the axial direction (XY plane). The hardness of each batch was tested with a Qness Q10 A hardness tester (ATM Qness GmbH, Austria) with a load of 10 N and a dwell time of 10 s. The hardness was measured in the middle of the specimen on a XY cut perpendicular to the build direction. The mean hardness was calculated by three depth profiles of five specimens for each batch. Specimens for the microstructural characterization were cut, embedded, ground down to a grid of 2400, polished and etched (99% ethanol and 1% nitric acid) before analysis on a LEO Gemini 1530 (Carl Zeiss AG, Germany) scanning electron microscope (SEM). An acceleration voltage of 10 kV and an aperture size of 60 µm was used in combination with a secondary electron detector (SE). The fracture surfaces were captured with a light microscope (Aristomet, Leica Microsystems GmbH, Germany). A Helios NanoLab 650 SEM (FEI, Thermo Fisher Scientific Inc., USA) featuring an e-Flash HD detector (Bruker Corporation, USA) was used for the electron backscatter diffraction (EBSD) analysis. The scans were carried out with an acceleration voltage of 20 kV and a beam current of 6.4 nA on a pre-tilted surface of 70°. The study utilized the MTEX 5.10.2 toolbox within MATLAB for analysis. For the austenite parent grain analysis, the total map resolution was set to 638 × 424 pixels with a step size of 600 nm and a 7 ms exposure time. Inverse pole figure (IPF) maps with highlighted parent grain boundaries were obtained with the method described by Niessen et al. [30]. The phase fraction and morphology analysis used EBSD scans with a total map resolution of 422 × 281 pixels at a step size of 50 nm and a 7 ms exposure time.

#### 2.3.2. X-ray diffraction

Besides the EBSD analysis, the retained austenite fraction was additionally determined through X-ray diffraction analysis (XRD). The diffraction patterns were recorded in Bragg–Brentano geometry with $\theta/\theta$ focusing, utilizing a D2 phaser (Bruker Corperation, USA). The X-ray tube with Cu-K$\alpha$ radiation with a wave length of $\lambda_{\mathrm{CuK}\alpha}$ = 1.5406 Å was operated at 30 kV and 10 mA. Scans were performed between 10° to 145° ($2\theta$). The $2\theta$ step size was set to 0.01° with an accumulated acquisition time of 384 s per step. To enhance the statistical data, the sample was rotated. In order to determine the retained austenite fraction, the four peak method according to the ASTM E975 standard was used [31].

The residual stresses in axial and tangential direction were determined using the X-ray diffraction method $\sin^2(\psi)$ with the material parameters $E_{211}$ = 211 GPa and $\nu_{211}$ = 0.3. The diffractometer DR45 (Stresstech GmbH, Germany) was used with Cr-K$\alpha$ radiation (30 kV and 9 mA) to measure the {211} $\alpha$-Fe diffraction line at 11 $\Psi$-angles between −45° and 45° in the modified $\chi$ mode. For all measurements, an exposure time of 10 s and a collimator with a beam diameter of 1 mm was used. The depth resolved residual stress analysis of the specimen was carried out by sequential electro chemical material removal using the Struers MoviPol-2 polishing device (Struers, Denmark).

#### 2.3.3. Mechanical testing

Fatigue testing was carried out using a moment-controlled rotating bending machine. The experiments were conducted with a constant frequency of 50 Hz and a load ratio of $R = -1$. The SN-curve was determined using a combination of the staircase method (at least 15 samples per batch) and the horizon method (at least 4 samples per load level). The tensile tests were conducted at room temperature using a Zwick/Roell 1484 universal testing machine (ZwickRoell AG, Germany) with a 200 kN load cell. A strain rate of $4 \times 10^{-4}\,\mathrm{s}^{-1}$ was used and the strain was measured using a sensor arm extensometer (ZwickRoell AG, Germany). Four specimens of each batch were tested. The toughness was calculated by numerical integration of each individual stress–strain curve.

### 2.4. Thermal simulation

To estimate the influence of the three different base plate preheating temperatures on the cooling rate and the resulting phase transformations, a simplified steady-state thermal model based on the model of Schüßler et al. [20] was created. In contrast to the model of Schüßler et al. [20], this finite element simulation focused solely on the energy input from the base plate preheating system while disregarding the laser's energy contribution to minimize computation expenses. While this approach simplifies calculations and enables a more computationally efficient analysis, it assumes uniform temperature distribution within each layer and does not account for localized thermal gradients caused by the laser's layer-by-layer interaction. As a result, the model may underestimate peak localized temperatures and cooling rates near the melt pool. This model therefore estimates only the minimum steady-state temperature expected during the process to predict the possible microstructure during cooling. The base plate preheating was modeled as a constant temperature boundary condition on the bottom surface of the base plate. Additionally, a constant heat transfer coefficient $h$ ($20\,\mathrm{W\,m^{-2}\,K^{-1}}$ [32]) was added on the top surface of each part as a boundary condition. This coefficient was coupled with the surface temperature $T$ in Kelvin and the ambient air temperature $T_{air}$, which corresponds to room temperature, specifically 293.16 K (Eq. (1)). The dissipation of heat through radiation was modeled with an emissivity $\varepsilon$ of 0.5 [32], the Stefan–Boltzmann constant $\sigma$, the surface temperature $T$ in Kelvin, and the air temperature $T_{air}$ in Kelvin (Eq. (2)).

$$q_{conv.} = h(T - T_{air}) \tag{1}$$

$$q_{rad.} = \varepsilon\sigma(T^4 - T_{air}^4) \tag{2}$$

Since the surface temperature is mainly dependent on the combination of thermal conductivity and the convection at the surface, the surface temperature is only slightly influenced by the specimens height. Therefore, the minimum surface temperatures reported in this paper were determined at the specimens' maximum height (worst case scenario). Future studies could enhance accuracy by incorporating laser energy input into the model to account for its effects on local cooling rates and phase transformations.

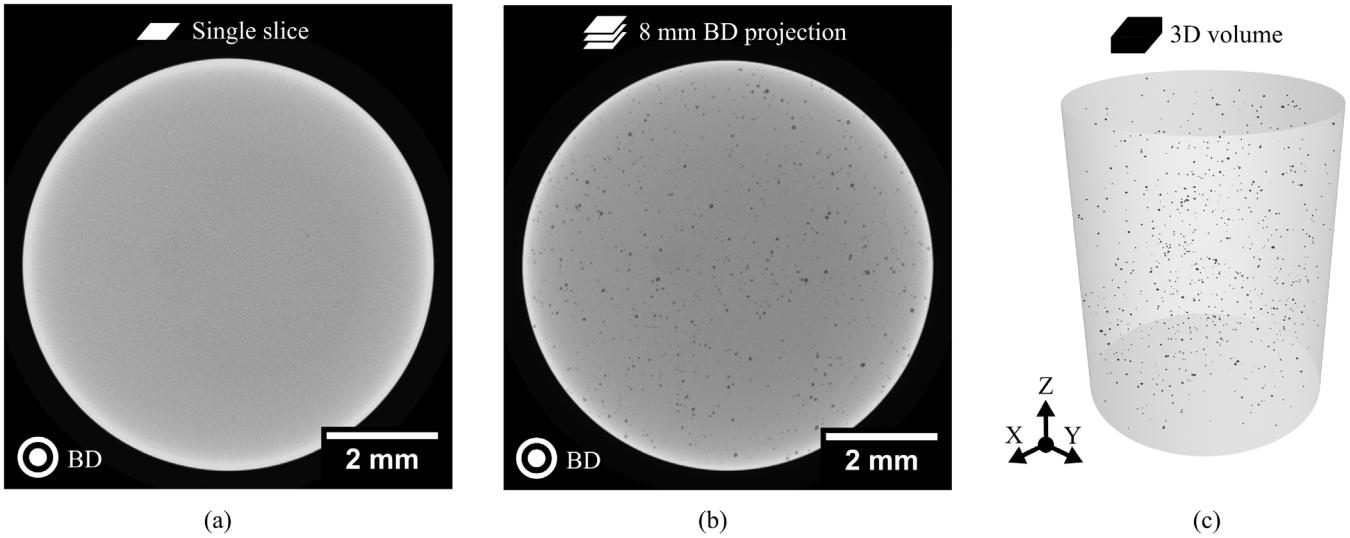


**Fig. 2.** (a) Single reconstructed $\mu$CT slice highlighting all pores in this 2D slice, (b) representative minimal grey value projection of all 2D slices (cumulative height of 8 mm) in build direction highlighting all pores of the 3D volume and (c) a full 3D representation of the same volume.

**Table 2**
Measured density and surface roughness in axial direction after machining. Mean values with standard deviation.

| Batch | Density/g cm$^{-3}$ | Surface roughness $R_z$/µm |
|---|---|---|
| Control-QT-M | 7.827 ± 0.003 | 5.53 ± 0.99 |
| AM150-M | 7.826 ± 0.003 | 6.60 ± 0.62 |
| AM300-M | 7.831 ± 0.006 | 5.05 ± 0.76 |
| AM450-M | 7.835 ± 0.006 | 6.48 ± 0.97 |

## 3. Results

### 3.1. Density and surface roughness

The density of components fabricated through AM is a crucial factor that is closely connected to the selected process strategy. Although the baseplate preheating temperatures altered the cooling rates, there were no notable differences in the measured densities across the various batches (Table 2).

Additionally, the average densities of all AM parts were comparable to those of the control batch made using traditional subtractive manufacturing methods. Of the batches examined, the lowest mean density was recorded for batch AM150-M with a value of 7.826 g cm$^{-3}$, while the highest was observed for batch AM450-M with 7.835 g cm$^{-3}$. The overlapping standard deviation of the density measurements indicated that the process variations had minimal effect on the final density of the parts. Therefore, no influence of baseplate preheat temperatures on part densities could be identified. Inspection of the specimens by $\mu$CT revealed the presence of a small number of spherical pores, likely to be gas pores (Fig. 2). The mean pore sphericity was calculated to 0.84 with a standard deviation of 0.03. However, no evidence of lack of fusion pores was found. This further confirms the high density and non-critical morphology of the manufactured parts. In order to focus on characterizing the bulk material properties rather than the surface state, all samples were machined to their final shape prior to testing. Following this machining step, the surface roughness was found to be similar across all batches, independent on the previous manufacturing process (Table 2).

### 3.2. Thermal simulation

Steady-state thermal simulations were conducted to predict surface temperatures during the additive manufacturing process. The analysis revealed a consistent and quasi-linear decrease in surface temperature as the specimen height increased (Fig. 3). At maximum specimen height, the surface temperatures reached their lowest values, with reductions of 47 °C for AM450-M specimens, 24 °C for AM300-M specimens and 9 °C for AM150-M specimens. These minimum temperatures were used as reference points to assess the worst-case scenario.

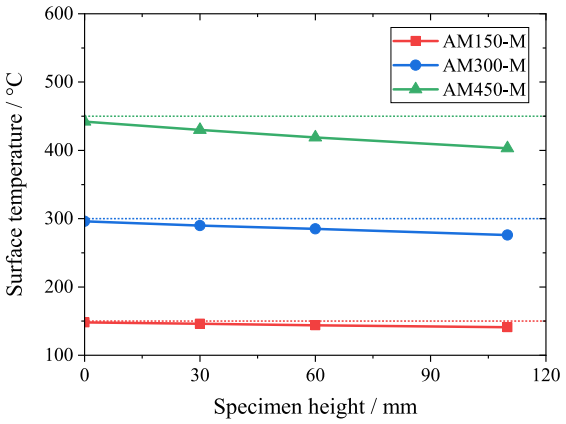


**Fig. 3.** Predicted surface temperatures at different specimen heights for the AM150-M, AM300-M and AM450-M specimens.

### 3.3. Residual stresses

Residual stress profiles were examined in both the axial (parallel to the build direction) and circumferential orientations from the surface down to a depth of 1.75 mm, revealing no significant differences among the four material conditions (Fig. 4). These residual stresses were largely influenced by the machining process, which induced compressive stresses near the surface, reaching up to 650 MPa. Following a distance of 100 µm to 200 µm, the compressive residual stresses transition to mildly tensile residual stresses, extending into the core of the specimen.

### 3.4. Hardness

The hardness depth profile was examined along the XY-plane, which runs perpendicular to the build direction for the additive manufacturing material states. A reduction in hardness occurs as the base plate

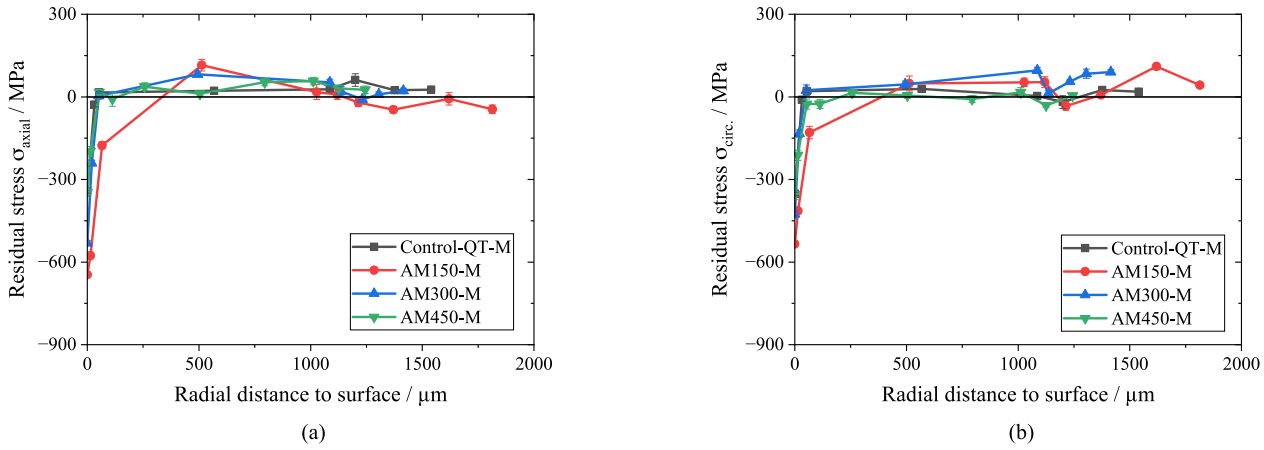


**Fig. 4.** Residual stress depth profile in (a) axial and (b) circumferential orientation along a radial path. The material was removed in steps by electro chemical etching.

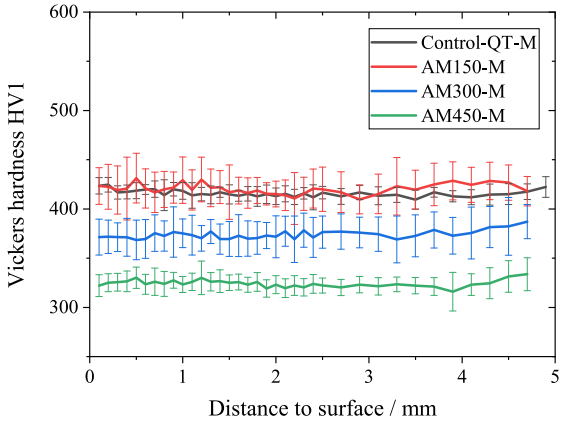


**Fig. 5.** Visualization of the measured hardness depth profile for all four batches. Measured on the XY cross section perpendicular to the build direction.

preheating temperature is increased (Fig. 5). The Vickers hardness values for the Control-QT-M and AM150-M specimens were found to be similar, with an average Vickers hardness of (416 ± 3) and (420 ± 5) respectively. No discernible trend was observed across the diameter of the samples, indicating a homogeneous distribution of hardness. In contrast, the AM300-M specimen, which was manufactured with a higher base plate preheating temperature, exhibited a slightly lower Vickers hardness of (374 ± 11). The AM450-M batch exhibited a more pronounced reduction in hardness, with a mean Vickers hardness of (316 ± 6). Additionally, the hardness depth profile along the build direction revealed a homogeneous hardness distribution.

### 3.5. Microstructure

#### 3.5.1. Phase fraction analysis

The resulting phase fractions were analyzed using both XRD and SEM-EBSD, with results from the two techniques showing strong agreement. Table 3 provides a summary for the calculated retained austenite phase fractions, while Fig. 6 illustrates the XRD intensity as a function of the 2$\theta$ angle.

For the Control-QT-M specimen, retained austenite levels were found to be below 2%. In contrast, the AM150-M specimen, produced via additive manufacturing, showed a retained austenite content of approximately 4 % to 5 %, despite having a similar bulk hardness to the Control-QT-M batch. SEM-EBSD imaging revealed small retained austenite blocks with a diameter of less than 1 µm dispersed in between the martensite laths. For the AM300-M and AM450-M specimens, both XRD and SEM-EBSD analyses indicated retained austenite levels

**Table 3**
Direct comparison of the measured retained austenite phase fraction (RA) by XRD and SEM-EBSD methods.

| | XRD/%RA | SEM-EBSD/%RA |
|---|---|---|
| Control-QT-M | <1.0 | 2.0 |
| AM150-M | 5.5 | 4.3 |
| AM300-M | <1.0 | 1.0 |
| AM450-M | <1.0 | 1.4 |

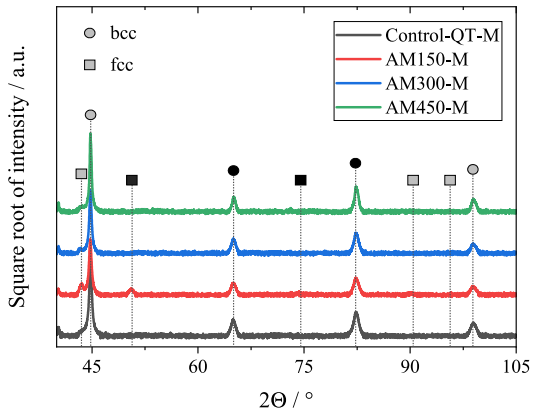


**Fig. 6.** XRD results of the specimens in the as-built (AM150-M, AM300-M, AM450-M) and Control batch (Control-QT-M). Calculated bcc and fcc peak positions were marked with circles and squares respectively. Positions used for the calculation of the retained austenite fraction were filled in black.

of less than 2%. The primary distinction between these specimens and the AM150-M is the base plate preheating temperature, which was increased to 300 °C and 450 °C for AM300-M and AM450-M, respectively.

#### 3.5.2. Grain and texture analysis

Parent grain reconstruction via SEM-EBSD analysis provided insight into the grain morphology and orientation across different batches, showing notable variations dependent on processing route and thermal history. While none of the analyzed batches showed a global texture, differences for the austenite parent grain morphology were noted. For the Control-QT-M batch, which was quenched and tempered, the reconstructed parent grains were primarily equiaxed. These grains exhibited a relatively small mean size of (6.04 ± 4.01) µm, as shown in Fig. 7(a). The equiaxed morphology of these grains is consistent with literature for a conventional quench and tempering route. In contrast, the AM150-M and AM350-M batches, displayed predominantly columnar parent grains after reconstruction. A pronounced orientation parallel

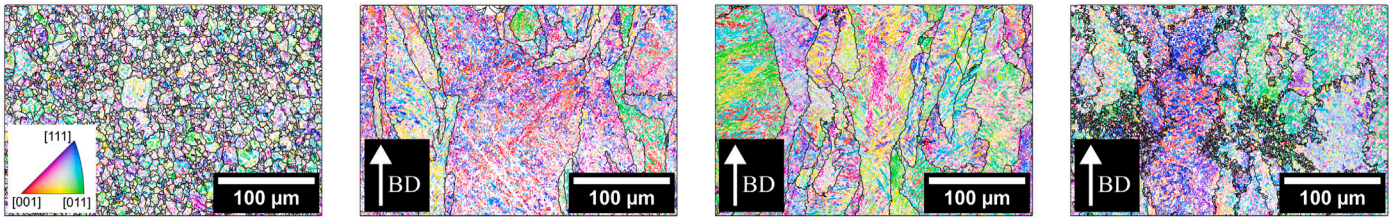


(a) Control-QT-M (b) AM150-M (c) AM300-M (d) AM450-M

**Fig. 7.** SEM-EBSD orientation images with IPF color key parallel to the build direction, overlayed by the reconstructed austenite parent grain boundaries. (For interpretation of the references to color in this figure legend, the reader is referred to the web version of this article.)

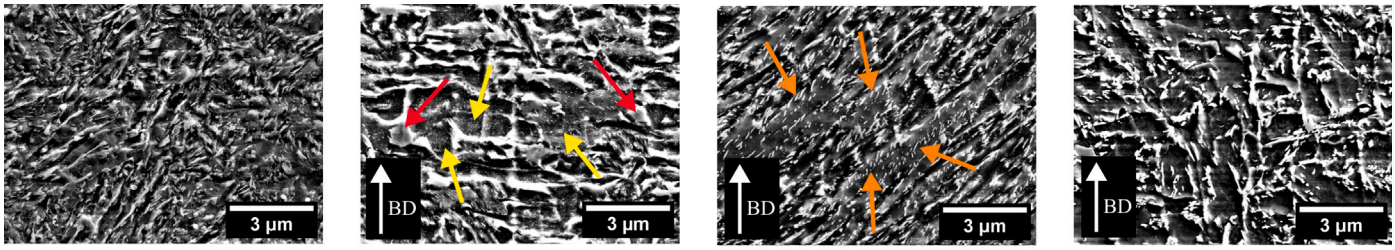


(a) Control-QT-M (b) AM150-M (c) AM300-M (d) AM450-M

**Fig. 8.** SEM-SE micrograph images of a cut section parallel to the build direction for the (a) Control-QT-M batch and (b-d) all three AM batches. Specimens were polished and etched with nital etchant. Representative islands of retained austenite were highlighted with red arrows, fine carbide precipitations with yellow arrows and the carbide precipitations at a 57° angle with the orange arrows. (For interpretation of the references to color in this figure legend, the reader is referred to the web version of this article.)

to the build direction was noted. The columnar grains observed in these AM batches were considerably larger than those in the quenched-and-tempered (QT) samples, as illustrated in Fig. 7(b) and (c). These larger, elongated grains align along the build direction due to the cyclic reheating and solidification inherent to the AM process, which promotes uniaxial grain growth over multiple layers. The AM450-M batch shows mainly columnar grains oriented in the build direction with regions of significantly smaller and less elongated grains in between (Fig. 7(d)). While the grains were found to be elongated parallel to the build direction, no distinct texture was found. The orientation of the reconstructed parent grains seems to be equally distributed.

### 3.5.3. Morphology analysis

Microstructural morphology analysis of the control and AM specimens was performed using SEM and EBSD images. The microstructure of Control-QT-M was consistent with typical quenched and tempered steels, displaying tempered martensite laths with dispersed precipitates as observed in the SEM (Figs. 8(a), 9(a) and (e)). The heat treatment applied resulted in a fully homogenized microstructure.

In contrast, the as-built AM150-M batch exhibited a microstructure shaped by the unique thermal cycling of the AM process, with rapid heating and cooling across successive layers. Thermal simulations estimated the minimum surface temperature to approximately 141 °C due to heat losses, which is insufficient to further temper the as-built microstructure (See Fig. 3). SEM-SE imaging revealed tempered martensite laths with small, intra-lath precipitates, although their small size made carbide indexing in SEM-EBSD less reliable (Figs. 8(b), 9(b) and (f)). Literature suggests that intrinsic tempering may lead to preferential carbide nucleation along grain boundaries in these as-built samples [20,33,34]. SEM-EBSD analysis also identified blocks of retained austenite (high pattern quality) in between the martensite laths (Fig. 9(b)).

For the AM300-M specimen, the combination of a base plate preheating temperature of 300 °C and the cyclic thermal profile from additive manufacturing resulted in a mixed microstructure of martensite and lower bainite. This suggests a significantly lower cooling rate in the bainite start temperature, even though the calculated minimal surface temperature of 276 °C remained below the martensite start temperature of 363 °C. The structure of the AM300-M lath appeared relatively coarse compared to the AM150-M (Fig. 9(g)). Carbide precipitations were observed along the lath boundaries, as well as with a distinct angle 57° within the laths, indicative of the morphology of lower bainite described in the literature [35,36] (Fig. 8(c)). Small clusters of retained austenite were observed in between the bainite and martensite laths, although smaller and fewer compared to the AM150-M microstructure (Fig. 9(c)).

Finally, the microstructure of AM450-M reflected the influence of even higher baseplate preheating, estimated at 403 °C by the thermal simulation. This temperature exceeds the martensite start temperature and results in a fully bainitic microstructure with an additional prolonged thermal exposure. The effects of elevated preheating temperatures and sustained cyclic heating on the final microstructure of the material are highlighted. Similar to a conventional austempering process route, this batch exhibited a coarser plate like bainitic matrix with cementite precipitates and a low amount of retained austenite (Figs. 8(d), 9(d) and (h)) [37]. Moreover, microscopic imperfections appeared as spherical inclusions approximately 1 µm in size in the Control-QT-M specimens. Furthermore, sparsely distributed former melt pool boundary regions with higher retained austenite levels were noted across all AM states.

### 3.6. Static mechanical properties

The tensile test results reveal distinct trends across the different material batches, highlighting the trade off between strength and ductility. The control specimen Control-QT-M and additive manufactured AM150-M exhibited similar mechanical properties, particularly in terms of proof stress ($R_{p0.2}$), ultimate tensile strength ($UTS$), elongation at fracture ($A$), and calculated toughness ($U_T$). Both batches showed a high level of tensile strength and balanced ductility, with only slight variations. The static mechanical properties were not significantly affected by the porosity of the AM route. However, a significant reduction in both $R_{p0.2}$ and $UTS$ was observed for the AM300-M batch (Table 4). Despite this decrease in strength, the elongation to fracture remained similar to the control. However, it still resulted in a minimum in toughness values for AM300-M. In contrast, the AM450-M batch

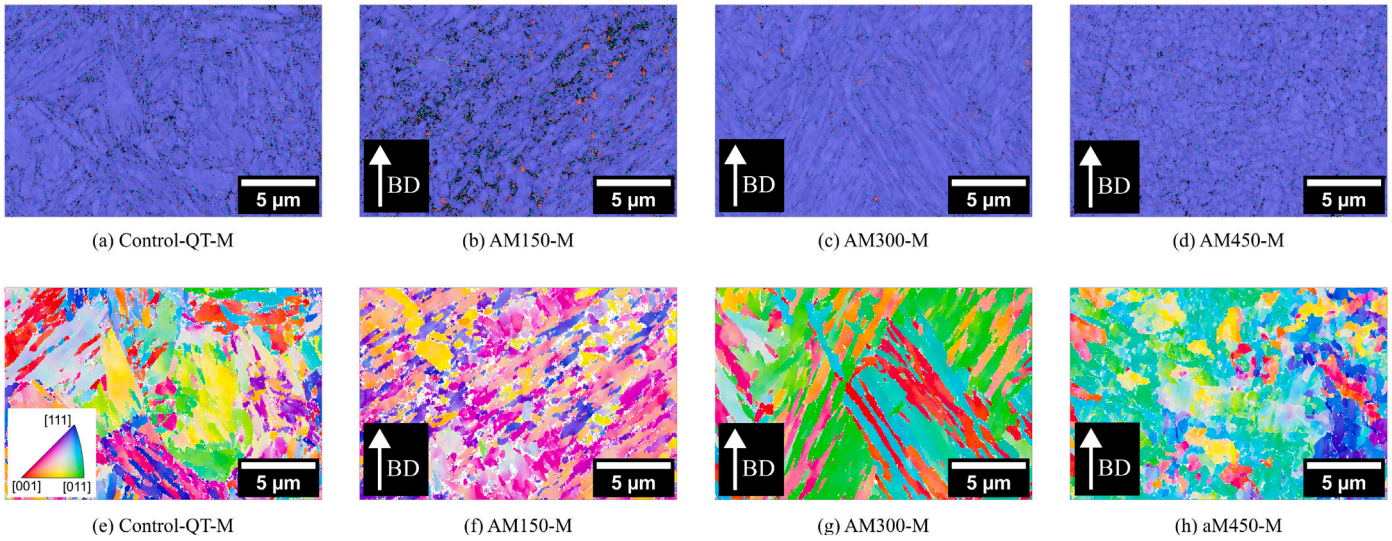


**Fig. 9.** High resolution SEM-EBSD (a)–(d) phase maps with overlayed band contrast. Bcc phase fraction are visualized in blue, fcc in red and cementite in light blue. As well as (e)–(h) the SEM-EBSD orientation images of the bcc phase fraction with IPF color key parallel to the build direction. (For interpretation of the references to color in this figure legend, the reader is referred to the web version of this article.)

**Table 4**
Direct comparison for the measured mean proof stress $R_{p0.2}$, ultimate tensile strength $UTS$ and elongation at fracture $A$ as well as the calculated toughness for all four batches.

| | $R_{p0.2}$/MPa | $UTS$/MPa | $A$/– | $U_T$/MJ m$^{-3}$ |
|---|---|---|---|---|
| Control-QT-M | 1271 ± 6 | 1350 ± 8 | 0.186 ± 0.01 | 225 ± 12 |
| AM150-M | 1156 ± 7 | 1315 ± 7 | 0.199 ± 0.01 | 242 ± 3 |
| AM300-M | 986 ± 22 | 1125 ± 28 | 0.180 ± 0.01 | 188 ± 3 |
| AM450-M | 874 ± 47 | 1017 ± 22 | 0.265 ± 0.02 | 250 ± 14 |

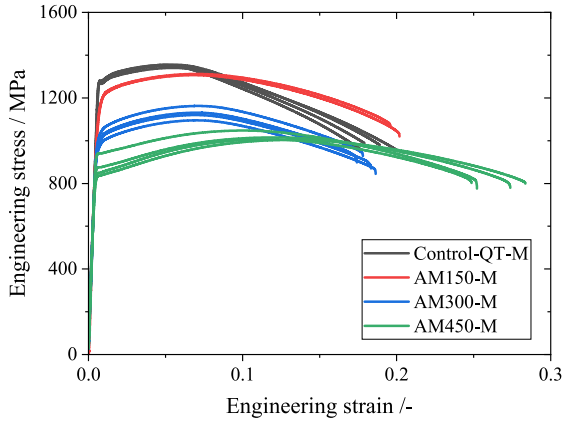


**Fig. 10.** Engineering stress–strain curves for all four batches.

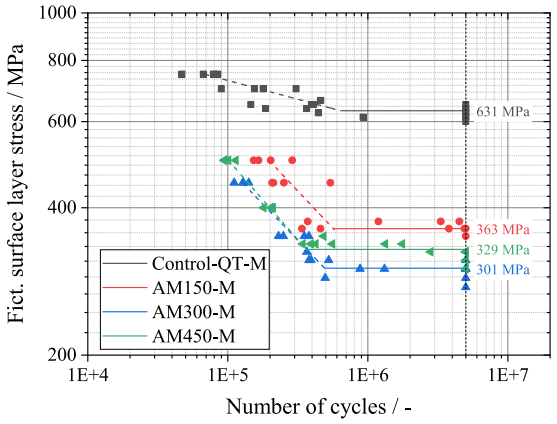


**Fig. 11.** SN-curves of rotational bending test ($R = -1$) of the AM batches (AM150-M, AM300-M and AM450-M) as well as the reference Control-QT-M batch for direct comparison with the AM150-M batch.

demonstrated even lower $R_{p0.2}$ and $UTS$, yet it exhibited a markedly higher elongation at fracture. This increase in ductility translated into a higher toughness value for AM450-M, surpassing both AM300-M and AM150-M (Fig. 10). Overall, while the control and AM150-M specimens maintained the highest strength, AM450-M's enhanced elongation suggests a favorable trade-off between strength and ductility, leading to superior toughness compared to AM300-M.

### 3.7. Fatigue properties

The fatigue properties of the tested materials demonstrate clear distinctions between the control and additively manufactured (AM) batches with regard to low-cycle fatigue (LCF) and high-cycle fatigue (HCF) strengths (Fig. 11). The control specimen (Control-QT-M) demonstrated a HCF strength of 631 MPa. This value is consistent with those reported in the literature for similar materials and heat treatments, confirming its superior fatigue resistance [38–41]. In contrast, the AM specimens exhibited comparable LCF strength across all batches, despite variations in base plate preheating temperatures, while showing significant differences in the HCF regime. Among the AM batches, AM150-M exhibited the highest HCF strength ($S_{e,50\%}$ = 363 MPa). However, this value represented a 40% reduction compared to Control-QT-M, despite similar hardness and mechanical properties. Similar HCF strength was reported in literature for AISI 4140 with a porosity of less than 1% [18], while an increase of porosity resulted in a reported HCF strength at least 6 times lower [18,19]. The HCF strength for AM300-M was the lowest at 301 MPa, while AM450-M exhibited an intermediate value of 329 MPa.

### 3.8. Fractography

The analysis of the fracture surfaces provides valuable insights into the mechanisms that limit the service life of the tested materials. In the case of the Control-QT-M specimens, the initial formation of cracks was predominantly observed at the surface (Fig. 12(a)), similar crack initiation sites were reported in literature [40,41]. This indicates that the

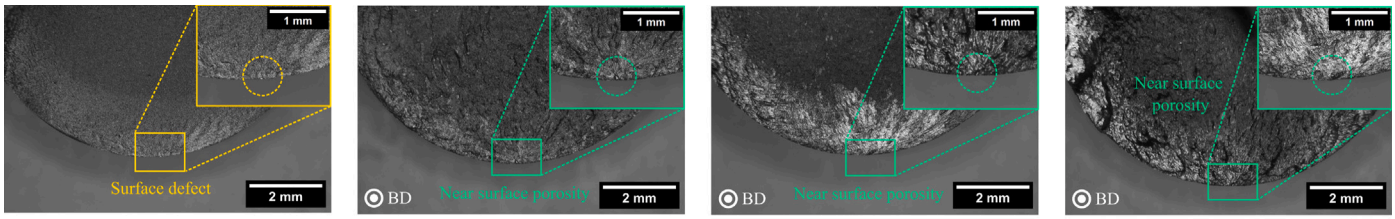


(a) Control-QT-M (b) AM150-M (c) AM300-M (d) AM450-M

**Fig. 12.** Fractografic light optical microscope images visualizing the characteristic (a) surface defects for the Control-QT-M batch, (b)–(d) near surface porosity for the AM150-M, AM300-M and AM450-M batches as the causes for failure.

minimization of surface defects is a crucial factor in the enhancement of fatigue performance in conventionally treated materials. In contrast, the AM batches exhibited crack initiation primarily at pores located in the vicinity of the surface (Fig. 12(b)–(d)). These pores, whether open or closed after turning the specimens to their final shape, were typically small and had a spherical morphology. There was no visible unmelted powder, indicating that they were likely caused by gas porosity rather than incomplete fusion. The presence of these pores resulted in the formation of localized stress concentrations. This effectively increased the notch factor, rendering them a more critical factor in fatigue failure than surface roughness. While the more spherical gas pores noted for this study increase the stress concentrations, lack of fusion porosity was linked to a more pronounced decrease of HCF strength in literature [18,19].

## 4. Discussion

### 4.1. Influence of base plate preheating temperature on fatigue strength

The additive manufacturing (AM) process with different base plate preheating temperatures resulted in similar porosity, surface roughness, and residual stress depth profiles. However, there were significant differences in microstructure and key properties such as hardness and toughness between the batches. As the processing steps were identical across all three batches with the sole exception being the preheating temperature of the base plate, any differences in the final properties can be linked to the base plate preheating temperature variation. The surface temperature and hardness depth profile remained unaffected by variations in build height (Refer to Sections 2.4 and 3.4). In AM, the process itself acts as a high-temperature, cyclic tempering effect for successive printed layers [3,20]. Base plate preheating adds an additional isothermal autotempering or austempering aspect to this thermal cycling by maintaining a steady elevated temperature throughout the printing process. The preheating temperature not only influences this isothermal tempering effect, but also modifies the cooling rate, thereby altering the minimum quenching temperature. Consequently, these conditions shift the transformation mechanisms over a range of different microstructures: from a predominantly martensitic transformation to a mixed martensitic-bainitic transformation and finally to a fully bainitic transformation. Higher baseplate preheating temperatures may also allow for ferritic transformation.

In the AM150-M batch, preheating created an autotempering effect on the martensitic matrix due to prolonged exposure to elevated temperatures, a phenomenon well documented in martensitic steels [42,43]. In the AM300-M batch, the transformation resembled an austempering process near the martensite start temperature, resulting in a mixed martensitic and lower bainite matrix. The reduced amount of retained austenite compared to the AM150-M batch can be explained by the extended soak time, as reported in literature [37]. Finally, the AM450-M batch showed characteristics similar to a conventional austempering process, with a coarser, plate-like upper bainite matrix with cementite precipitates and minimal retained austenite [37]. As the preheating temperature of the base plate rises, the transformation temperature also increases, leading to a decrease of the resulting hardness (Fig. 5).

The observed minimum in fatigue strength for the AM300-M batch can be linked to tempered martensite embrittlement (TME). Typically, TME occurs in quenched and tempered steels (QT) when tempered in the 200 °C to 400 °C range [28,29]. This phenomenon was first explored by Kula et al. [44] for AISI 4340 and was later elaborated for different low-carbon steels (see for example Refs. [45–50]) and recently summarized by George Krauss [29]. This embrittlement reduces toughness, leading to brittle failure modes — a phenomenon typically mitigated by tempering at 200 °C for maximum hardness (low temperature tempering LTT) or above 400 °C for improved ductility (high temperature tempering HTT) [28,29,51]. TME is typically associated with the precipitation of coarse interlath cementite [29,33,50,52–55] due to the decomposition of retained austenite while the replacement of fine transition carbides by intralath cementite does not appear to influence the toughness [29,54]. Damon et al. [3] demonstrated a correlation between hardness and volume energy density (VED) in AM processes, comparing it with the tempering temperatures needed to achieve equivalent hardness in conventional processes. Using Hollomon and Jaffe's equations [56], the AM300-M batch's mean hardness of 375 Vickers corresponds to a conventional equivalent tempering temperature of approximately 520 °C for two hours — well above the TME range. Nevertheless, results for the AM300-M batch's toughness and fatigue strength suggest a significant embrittlement effect due to prolonged exposure to the elevated base plate preheating temperature, initiating an additional tempering step. This autotempering involves carbon redistribution from supersaturated ferrite into residual austenite and the precipitation of carbides, which are characteristic features of bainite formation [57]. Consequently, this increases the amount of retained austenite. Since no retained austenite was measured by XRD and SEM-EBSD analysis, this study indicates that the combination of the inherent thermal cycling of the AM process and prolonged exposure to the base plate preheating effectively transformed the retained austenite to cementite. Studies indicate that significant tempering effects in bainitic microstructure only start close to the austenite transformation temperature [26,27]. For the AM300-M batch, which contains a mixed martensitic and bainitic microstructure, this suggests that the embrittlement effect observed arises mainly from the decomposition of retained austenite during the induced tempering process. While the literature suggests benefits for these conventionally processed mixed microstructures [24,25,58], the results of this study indicate that the extremely prolonged autotempering during the AM process enables the embrittlement.

The AM150-M batch, with a fully martensitic microstructure, experienced autotempering at temperatures likely too low to cause notable decomposition of retained austenite. This batch, with higher strength and comparable fracture elongation to the AM300-M batch, achieved greater toughness and correspondingly higher fatigue strength. Conversely, the AM450-M batch exhibited a fully bainitic, austempered microstructure. Given that bainitic autotempering occurs at elevated transformation temperatures, the literature indicates that no additional tempering effect should be expected for this batch's microstructure [26].

In summary, carbide precipitation due to retained austenite decomposition accounts for the reduction in toughness and, crucially, the lower fatigue strength of the AM300-M batch when compared to the AM150-M and AM450-M batches. The results highlight the importance of parameter selection for the PBF-LB AM process. Despite the lower measured hardness of the AM specimens, tempering in the known TME range will lead to a significant increase in embrittlement. The results indicate the advantage of a low base plate preheating temperature for a trade off between mitigating crack formation and favorable material properties. However, if higher ductility is required or if a higher base plate temperature is necessary to prevent cracking in more complex components, it must be ensured that the temperature does not fall within the TME range at critical points of the component. The base plate preheating temperature can therefore be a useful tool to integrate the required heat treatment into the AM process, mitigating the need for an additional processing step.

### *4.2. Influence of porosity and microstructure on fatigue strength*

Literature indicates that additive manufacturing (AM) significantly impacts four key properties: density or porosity, surface roughness, residual stress state, and microstructure [1,8]. However, isolating the influence of each factor is challenging due to the interconnected nature of these effects. For example, machining the specimen surface not only alters surface roughness but also removes porosity clusters near the surface and modifies the residual stress profile. In this study, comparative analysis between the AM150-M and Control-QT-M samples – both subjected to similar machining – revealed comparable surface roughness and residual stress states. However, two key differences emerged that notably affect mechanical properties: the microstructure and porosity. When both porosity and microstructural effects were considered, an overall reduction in fatigue strength of 42% was observed from the Control-QT-M to the AM150-M batch. Although the hardness levels were similar, distinct microstructural characteristics were observed in AM150-M. These include a finer carbide precipitate morphology, a higher retained austenite fraction, and a columnar grain structure oriented parallel to the applied fatigue test load, suggesting anisotropic material properties. In addition, inhomogeneities such as former melt pool boundaries with higher retained austenite levels were present. These features, rooted in thermal history and crystallization/transformation pathways, have implications for fatigue performance that are not adequately captured by macroscopic hardness alone. Differences were also noted for the measured porosity of the AM150-M compared to the Control-QT-M sample manufactured by the conventional route. Although the porosity levels in this study were relatively low and the pores detected were largely spherical, $\mu$CT imaging shows that even small amounts of porosity can act as localized notches that compromises fatigue strength. In this near-ideal scenario for AM parts, the observed effects underscore the likelihood of even more significant reductions in fatigue strength. This is particularly true for samples with greater bulk porosity or non-spherical pores, such as the lack of fusion pores [18]. While post-processing techniques such as hot isostatic pressing (HIP) can reduce porosity, they also alter the microstructure, adding further complexity to achieving optimal performance [4].

In summary, the observed reduction in fatigue strength of AM150-M compared to Control-QT-M highlights the combined effects of porosity and microstructure on mechanical performance. While machining mitigated surface roughness and altered residual stresses, the inherent porosity and columnar grain structure of AM specimens remained critical factors. Even low levels of spherical porosity acted as stress concentrators, reducing fatigue performance, with anisotropic microstructural features such as columnar grains and retained austenite zones further exacerbating the issue. These findings emphasize the need for precise control of porosity during the PBF-LB process to minimize its detrimental effects on fatigue strength. Techniques such as optimized laser scanning strategies or targeted post-processing (e.g., hot isostatic pressing) can reduce porosity but must be carefully balanced against potential changes to the microstructure. For applications requiring high fatigue performance, tailoring process parameters to achieve a refined, isotropic microstructure and minimizing porosity can significantly enhance service life. This approach enables the design of AM components with predictable and robust mechanical properties.

## 5. Conclusion

In conclusion, this study has demonstrated the influence of base plate preheating temperature on the microstructure, hardness, and fatigue performance of additively manufactured (AM) AISI 4140 steel by the laser powder bed fusion process. The following key findings highlight the implications for process optimization and fatigue performance:

- Effect of preheating temperature on microstructure: The base plate preheating temperature can be a useful tool to intrinsically tailor resulting material properties without the need of an additional process step. Varying base plate temperatures led to distinct microstructures, from fully martensitic microstructure with a base plate preheating temperature of 150 °C to a mixed martensitic-bainitic at 300 °C and fully bainitic structure at 450 °C, significantly influencing fatigue behavior. The batch with a base plate preheating temperature of 150 °C achieved the highest fatigue strength, followed by the batch with 450 °C. The lowest fatigue strength was measured at 300 °C base plate preheating temperature.
- Tempered martensite embrittlement (TME): The mixed martensitic-bainitic structure in AM300-M exhibited embrittlement, likely due to TME, which decreased toughness and fatigue resistance. Notably, the TME occurred within the same 200 °C to 400 °C temperature range for the AM process as expected for the slower conventional quench and tempering process. However, the batch with a base plate preheating temperature of 300 °C exhibited TME effects at a significantly lower bulk hardness due to inherent thermal cycling and prolonged exposure during additive manufacturing.
- Comparison to conventional process route: For the comparison of the AM and conventional process route, the influence of residual stresses and surface roughness was eliminated by an additional machining process. The difference between the AM and conventionally manufactured control batches were therefore directly attributed to the influence of the combination of microstructure and porosity. A reduction of 42% in fatigue strength was noted. For applications requiring high fatigue performance, tailoring process parameters to achieve a refined, isotropic microstructure and minimizing porosity can significantly enhance service life.

These findings emphasize that careful control of both porosity and microstructure through additive manufacturing parameters is essential for enhancing the fatigue performance of AISI 4140 steel components. Small changes of process parameters can significantly influence the resulting properties. Future research should focus on refining these parameters to balance strength, ductility, and fatigue resistance, broadening the material's application in high-performance engineering fields.

## Declaration of Generative AI and AI-assisted technologies in the writing process

During the preparation of this work the authors used DeepL (DeepL SE, Germany) and Writefull (Writefull, UK) in order to improve the readability and language of the manuscript. After using these tools, the authors reviewed and edited the content as needed and take full responsibility for the content of the publication.

## Funding

Funded by the Deutsche Forschungsgemeinschaft (DFG, German Research Foundation) – SFB 1574–471687386.

## Declaration of competing interest

The authors declare that they have no known competing financial interests or personal relationships that could have appeared to influence the work reported in this paper.

## Acknowledgments

The authors would like to thank the Institute for Applied Materials (IAM-ZM) at the Karlsruhe Institute of Technology (KIT) for the use of the SEM-EBSD. The authors acknowledge the chemical analysis by ICP-OES conducted at the Institute for Applied Materials (IAM-AWP), Karlsruhe Institute of Technology (KIT).

## References

[1] Yadollahi A, Shamsaei N. Additive manufacturing of fatigue resistant materials: Challenges and opportunities. Int J Fatigue 2017;98:14–31. http://dx.doi.org/10.1016/j.ijfatigue.2017.01.001.

[2] Meneghetti G, Rigon D, Gennari C. An analysis of defects influence on axial fatigue strength of maraging steel specimens produced by additive manufacturing. Int J Fatigue 2019;118:54–64. http://dx.doi.org/10.1016/j.ijfatigue.2018.08.034.

[3] Damon J, Koch R, Kaiser D, Graf G, Dietrich S, Schulze V. Process development and impact of intrinsic heat treatment on the mechanical performance of selective laser melted AISI 4140. Addit Manuf 2019;28:275–84. http://dx.doi.org/10.1016/j.addma.2019.05.012.

[4] Damon J, Czink S, Schüßler P, Antusch S, Klein A, Send S, Dapprich D, Dietrich S, Schulze V. Mechanical surface treatment of EBM Ti6Al4V components: Effects of the resulting surface layer state on fatigue mechanisms and service life. Mater Sci Eng A 2022;849:143422. http://dx.doi.org/10.1016/j.msea.2022.143422.

[5] Yadollahi A, Shamsaei N, Thompson SM, Seely DW. Effects of process time interval and heat treatment on the mechanical and microstructural properties of direct laser deposited 316L stainless steel. Mater Sci Eng A 2015;644:171–83. http://dx.doi.org/10.1016/j.msea.2015.07.056.

[6] Bartlett JL, Li X. An overview of residual stresses in metal powder bed fusion. Addit Manuf 2019;27:131–49. http://dx.doi.org/10.1016/j.addma.2019.02.020.

[7] Soyama H, Takeo F. Effect of various peening methods on the fatigue properties of titanium alloy Ti6Al4V manufactured by direct metal laser sintering and electron beam melting. Materials 2020;13(10):2216. http://dx.doi.org/10.3390/ma13102216.

[8] Fayazfar H, Salarian M, Rogalsky A, Sarker D, Russo P, Paserin V, Toyserkani E. A critical review of powder-based additive manufacturing of ferrous alloys: Process parameters, microstructure and mechanical properties. Mater Des 2018;144:98–128. http://dx.doi.org/10.1016/j.matdes.2018.02.018.

[9] Englert L, Czink S, Dietrich S, Schulze V. How defects depend on geometry and scanning strategy in additively manufactured AlSi10Mg. J Mater Process Technol 2022;299:117331. http://dx.doi.org/10.1016/j.jmatprotec.2021.117331.

[10] Bobel A, Hector LG, Chelladurai I, Sachdev AK, Brown T, Poling WA, Kubic R, Gould B, Zhao C, Parab N, Greco A, Sun T. In situ synchrotron X-ray imaging of 4140 steel laser powder bed fusion. Materialia 2019;6:100306. http://dx.doi.org/10.1016/j.mtla.2019.100306.

[11] Hearn W, Steinlechner R, Hryha E. Laser-based powder bed fusion of non-weldable low-alloy steels. Powder Metall 2022;65(2):121–32. http://dx.doi.org/10.1080/00325899.2021.1959695.

[12] Hearn W, Harlin P, Hryha E. Development of powder bed fusion – laser beam process for AISI 4140, 4340 and 8620 low-alloy steel. Powder Metall 2022;1–13. http://dx.doi.org/10.1080/00325899.2022.2134083.

[13] Hearn W, Hryha E. Effect of carbon content on the processability of Fe-C alloys produced by laser based powder bed fusion. Front Mater 2022;8:547. http://dx.doi.org/10.3389/fmats.2021.800021.

[14] Shi C, Dietrich S, Schulze V. Parameter optimization and mechanical properties of 42CrMo4 manufactured by laser powder bed fusion. Int J Adv Manuf Technol 2022;121(3–4):1899–913. http://dx.doi.org/10.1007/s00170-022-09474-9.

[15] Damon J, Dietrich S, Vollert F, Gibmeier J, Schulze V. Process dependent porosity and the influence of shot peening on porosity morphology regarding selective laser melted AlSi10Mg parts. Addit Manuf 2018;20:77–89. http://dx.doi.org/10.1016/j.addma.2018.01.001.

[16] Benedetti M, Torresani E, Leoni M, Fontanari V, Bandini M, Pederzolli C, Potrich C. The effect of post-sintering treatments on the fatigue and biological behavior of Ti-6Al-4V ELI parts made by selective laser melting. J Mech Behav Biomed Mater 2017;71:295–306. http://dx.doi.org/10.1016/j.jmbbm.2017.03.024.

[17] Balasubramanian N, Langdon TG. The strength–grain size relationship in ultrafine-grained metals. Metall Mater Trans A 2016;47(12):5827–38. http://dx.doi.org/10.1007/s11661-016-3499-2.

[18] Shi C, Nouri N, Schulze V, Dietrich S. High cycle fatigue behaviour of AISI 4140 steel manufactured by laser-powder bed fusion. Int J Fatigue 2023;168:107469. http://dx.doi.org/10.1016/j.ijfatigue.2022.107469.

[19] Shi C, Schulze V, Dietrich S. Influences of laser remelting on mechanical performances of AISI4140 steel. Mater Sci Technol 2024. http://dx.doi.org/10.1177/02670836231212614.

[20] Schüßler P, Nouri N, Schulze V, Dietrich S. A novel multiscale process simulation to predict the impact of intrinsic heat treatment on local microstructure gradients and bulk hardness of AISI 4140 manufactured by laser powder bed fusion. Virtual Phys Prototyp 2023;18(1):e2271455. http://dx.doi.org/10.1080/17452759.2023.2271455.

[21] Mertens R, Vrancken B, Holmstock N, Kinds Y, Kruth JP, Van Humbeeck J. Influence of powder bed preheating on microstructure and mechanical properties of H13 Tool Steel SLM Parts. Physics Procedia 2016;83:882–90. http://dx.doi.org/10.1016/j.phpro.2016.08.092.

[22] Mertens R, Dadbakhsh S, Humbeeck JV, Kruth JP. Application of base plate preheating during selective laser melting. In: Procedia CIRP. 10th CIRP conference on photonic technologies LANE 2018, vol. 74, 2018, p. 5–11. http://dx.doi.org/10.1016/j.procir.2018.08.002.

[23] Wang W, Kelly S. A metallurgical evaluation of the powder-bed laser additive manufactured 4140 steel material. JOM 2016;68(3):869–75. http://dx.doi.org/10.1007/s11837-015-1804-y.

[24] Chen J-Z, Zhang B, Zeng L-R, Song Z-M, She Y-Y, Zhang G-P. Optimal bainite contents for maximizing fatigue cracking resistance of bainite/martensite dual-phase EA4T steels. Steel Res Int 2018;89(7):1700562. http://dx.doi.org/10.1002/srin.201700562.

[25] Chen J, Zhang B. Effect of bainite volume fraction on fatigue properties of bainite/martensite dual phase EA4T steel. J Miner Met Mater Eng 2019;5:12–21.

[26] Ohmori Y, Ohtani H, Kunitake T. Tempering of the bainite and the bainite/martensite duplex structure in a low-carbon low-alloy steel. Met Sci 1974;8(1):357–66. http://dx.doi.org/10.1179/msc.1974.8.1.357.

[27] Ståhlkrantz A, Hedström P, Sarius N, Sundberg H-Å, Kahl S, Thuvander M, Borgenstam A. Effect of tempering on the bainitic microstructure evolution correlated with the hardness in a low-alloy medium-carbon steel. Metall Mater Trans A 2020;51(12):6470–81. http://dx.doi.org/10.1007/s11661-020-06030-6.

[28] Clarke AJ, Klemm-Toole J, Clarke KD, Coughlin DR, Pierce DT, Euser VK, Poplawsky JD, Clausen B, Brown D, Almer J, Gibbs PJ, Alexander DJ, Field RD, Williamson DL, Speer JG, Krauss G. Perspectives on quenching and tempering 4340 steel. Metall Mater Trans A 2020;51(10):4984–5005. http://dx.doi.org/10.1007/s11661-020-05972-1.

[29] Krauss G. Tempering of lath martensite in low and medium carbon steels: assessment and challenges. Steel Res Int 2017;88(10):1700038. http://dx.doi.org/10.1002/srin.201700038.

[30] Niessen F, Nyyssönen T, Gazder AA, Hielscher R. Parent grain reconstruction from partially or fully transformed microstructures in *MTEX*. J Appl Crystallogr 2022;55(1):180–94. http://dx.doi.org/10.1107/S1600576721011560.

[31] ASTM International. Standard test method for X-Ray determination of retained austenite in steel with near random crystallographic orientation. 2022, http://dx.doi.org/10.1520/E0975-22.

[32] Peyre P, Aubry P, Fabbro R, Neveu R, Longuet A. Analytical and numerical modelling of the direct metal deposition laser process. J Phys D: Appl Phys 2008;41(2):025403. http://dx.doi.org/10.1088/0022-3727/41/2/025403.

[33] Morsdorf L, Kashiwar A, Kübel C, Tasan C. Carbon segregation and cementite precipitation at grain boundaries in quenched and tempered lath martensite. Mater Sci Eng A 2023;862:144369. http://dx.doi.org/10.1016/j.msea.2022.144369.

[34] Nakamura Y, Mikami T, Nagakura S. In situ high temperature electron microscopic study of the formation and growth of cementite particles at the third stage of tempering of martensitic high carbon steel. Trans Japan Inst Met 1985;26(12):876–85. http://dx.doi.org/10.2320/matertrans1960.26.876.

[35] Bhadeshia HKDH. The lower bainite transformation and the significance of carbide precipitation. Acta Metall 1980;28(8):1103–14. http://dx.doi.org/10.1016/0001-6160(80)90093-0.

[36] Shimizu K, Ko T, Nishiyama Z. Transmission electron microscope observation of the bainite of carbon steel. Trans JIM 1964;5(4):225–30. http://dx.doi.org/10.2320/matertrans1960.5.225.

[37] Bilal MM, Yaqoob K, Zahid MH, ul haq E, Tanveer WH, Wadood A, Ahmed B. Effect of austempering conditions on the microstructure and mechanical properties of AISI 4340 and AISI 4140 steels. J Mater Res Technol 2019;8(6):5194–200. http://dx.doi.org/10.1016/j.jmrt.2019.08.042.

[38] Dietrich S, Heudorfer R, Schulze V. Process integration of innovative mechanical surface treatment methods with induction surface hardening. In: Proceedings of the 28th IFHTSE congress. 2023.

[39] Park HJ, Kim BS, Ahn CS, Cho KT, Moon KI, Kim SS. Fracture behavior of ion-nitrided AISI 4140 steel in accordance with variable applied current density. Adv Mater Sci Eng 2022;2022(1):6244566. http://dx.doi.org/10.1155/2022/6244566.

[40] Çelik A, Karadeniz S. Improvement of the fatigue strength of AISI 4140 steel by an ion nitriding process. Surf Coat Technol 1995;72(3):169–73. http://dx.doi.org/10.1016/0257-8972(94)02348-4.
[41] Jadhav P, Prasad R, Mane R, Ukhande M, Arangi S. Influence of heat treatment on fatigue and fracture toughness behavior of AISI 4140 steel. In: Proceedings of the 23rd IFHTSE congress. 2016.
[42] Cheng L, Brakman CM, Korevaar BM, Mittemeijer EJ. The tempering of iron- carbon martensite; dilatometric and calorimetric analysis. Metall Trans A 1988;19(10):2415–26. http://dx.doi.org/10.1007/BF02645469.
[43] Vieweg A, Povoden-Karadeniz E, Ressel G, Prevedel P, Wojcik T, Mendez-Martin F, Stark A, Keckes J, Kozeschnik E. Phase evolution and carbon redistribution during continuous tempering of martensite studied with high resolution techniques. Mater Des 2017;136:214–22. http://dx.doi.org/10.1016/j.matdes.2017.09.065.
[44] Kula EB, Anctil AA. Tempered martensite embrittlement and fracture toughness in 4340 steel. Technical report, Defense Technical Information Center; 1967, http://dx.doi.org/10.21236/AD0651066.
[45] Rellick JB, McMahon CJ. Intergranular embrittlement of iron-carbon alloys by impurities. Metall Trans 1974;5(11):2439–50. http://dx.doi.org/10.1007/BF02644027.
[46] Tauscher S, Thornton P. Temper embrittlement in 4140 seamless tubing. Technical report, US Army Armament Research and Development Command; 1977.
[47] Ritchie RO. Near-threshold fatigue crack propagation in ultra-high strength steel: influence of load ratio and cyclic strength. J Eng Mater Technol 1977;99(3):195–204. http://dx.doi.org/10.1115/1.3443519.
[48] Lee KS, Kwon H, Lee YC, Lee JH, Cho ND. Fracture behaviour in tempered martensite embrittlement of medium-carbon alloy steels. J Mater Sci 1987;22(12):4215–20. http://dx.doi.org/10.1007/BF01132011.
[49] Ohtani H, Okaguchi S, Fujishiro Y, Ohmori Y. Morphology and properties of low-carbon bainite. Metall Trans A 1990;21(3):877–88. http://dx.doi.org/10.1007/BF02656571.
[50] Darwish FA, Pereira LC, Gatts C, Graça ML. On the tempered martensite embrittlement in AISI 4140 low alloy steel. Mater Sci Eng A 1991;132:L5–9. http://dx.doi.org/10.1016/0921-5093(91)90388-4.
[51] Chuang JH, Tsay LW, Chen C. Crack growth behaviour of heat-treated 4140 steel in air and gaseous hydrogen. Int J Fatigue 1998;20(7):531–6. http://dx.doi.org/10.1016/S0142-1123(98)00019-X.
[52] Horn RM, Ritchie RO. Mechanisms of tempered martensite embrittlement in low alloy steels. Metall Trans A 1978;9(8):1039–53. http://dx.doi.org/10.1007/BF02652208.
[53] Tsuboi M, Shibata A, Terada D, Tsuji N. Role of different kinds of boundaries against cleavage crack propagation in low-temperature embrittlement of low-carbon martensitic steel. Metall Mater Trans A 2017;48(7):3261–8. http://dx.doi.org/10.1007/s11661-017-4107-9.
[54] Zia-Ebrahimi F, Krauss G. Mechanisms of tempered martensite embrittlement in medium-carbon steels. Acta Metall 1984;32(10):1767–78. http://dx.doi.org/10.1016/0001-6160(84)90233-5.
[55] Peters JA, Bee JV, Kolk B, Garrett GG. On the mechanisms of tempered martensite embrittlement. Acta Metall 1989;37(2):675–86. http://dx.doi.org/10.1016/0001-6160(89)90251-4.
[56] Hollomon JH, Jaffe LD. Time-temperature relations in tempering steel. Trans AIME 1945;162:223–49.
[57] Srinivasan GR, Wayman CM. The crystallography of the bainite transformation - I. Acta Metall 1968;16(5):621–36. http://dx.doi.org/10.1016/0001-6160(68)90136-3.
[58] Mühl F, Jarms J, Kaiser D, Dietrich S, Schulze V. Tailored bainitic-martensitic microstructures by means of inductive surface hardening for AISI 4140. Mater Des 2020;195:108964. http://dx.doi.org/10.1016/j.matdes.2020.108964.